Fermi surface reconstruction due to the orthorhombic distortion in Dirac semimetal YbMnSb₂

Dilip Bhoi, ¹ Feng Ye, ² Hanming Ma, ¹ Xiaoling Shen, ¹ Arvind Maurya, ³ Shusuke Kasamatsu, ⁴ Takahiro Misawa, ¹ Kazuyoshi Yoshimi, ¹ Taro Nakajima, ¹ Masaaki Matsuda, ² and Yoshiya Uwatoko ¹

¹ The Institute for Solid State Physics, University of Tokyo, Kashiwa, Chiba 277-8581, Japan
 ² Neutron Scattering Division, Oak Ridge National Laboratory, Oak Ridge, Tennessee 37831, USA
 ³ Department of Physics, School of Physical Sciences, Mizoram University, Aizawl 796 004, India
 ⁴ Academic Assembly (Faculty of Science), Yamagata University, Yamagata 990-8560, Japan
 (Dated: June 23, 2023)

Dirac semi-metal with magnetic atoms as constituents delivers an interesting platform to investigate the interplay of Fermi surface (FS) topology, electron correlation, and magnetism. One such family of semi-metal is YbMn Pn_2 (Pn = Sb, Bi), which is being actively studied due to the intertwined spin and charge degrees of freedom. In this Letter, we investigate the relationship between the magnetic/crystal structures and FS topology of YbMnSb₂ using single crystal x-ray diffraction, neutron scattering, magnetic susceptibility, magnetotransport measurement and complimentary DFT calculation. Contrary to previous reports, the x-ray and neutron diffraction reveal that YbMnSb₂ crystallizes in an orthorhombic Pnma structure with notable anti-phase displacement of the magnetic Mn ions that increases in magnitude upon cooling. First principles DFT calculation reveals a reduced Brillouin zone and more anisotropic FS of YbMnSb₂ compared to YbMnBi₂ as a result of the orthorhombicity. Moreover, the hole type carrier density drops by two orders of magnitude as YbMnSb₂ orders antiferromagnetically indicating band folding in magnetic ordered state. In addition, the Landau level fan diagram yields a non-trivial nature of the SdH quantum oscillation frequency arising from the Dirac-like Fermi pocket. These results imply that YbMnSb₂ is an ideal platform to explore the interplay of subtle lattice distortion, magnetic order, and topological transport arising from relativistic quasiparticles.

Magnetic Dirac/Weyl semimetals deliver a promising platform, where the novel coupling between magnons and relativistic fermions could be exploited to manipulate the quantum transport phenomena using various parameters like chemical substitution, pressure, strain, etc. In this context, the collinear antiferromagnetic (AFM) ternary $A\text{Mn}Pn_2$ (where A = rare earth elements like Eu, Yb or alkali earth elements like Ca, Sr, Ba; Pn = pnictides Sb or Bi) have attracted increasing attention due to the presence of anisotropic Dirac cones close to the Fermi level, $E_{\rm F}$ [1–16].

The 112-type $AMnPn_2$ consists of a stacking of twodimensional (2D) Pn conduction layers, A-layers, and insulating $MnPn_4$ layers as shown in Fig.1(a). In $MnPn_4$ layers, each Mn atom is surrounded by four Pn atoms forming a tetrahedron, whereas 2D-Pn layers are responsible mostly for the exotic properties like quantum magnetoresistance [1–6] and bulk quantum Hall effect [16–18]. Band structure calculations revealed that the electronic density of states at $E_{\rm F}$ is primarily composed of the Pn $p_{x/y}$ and Mn-d orbitals, suggesting a close relationship between the Mn moment direction and underlying electronic structure [19–23]. Interestingly, these calculations further predict that the FM component arising from a canting of Mn moments breaks the time-reversal symmetry, thus playing a vital role in producing different topological states depending on the Mn moment direction [15, 19–24].

Among the 112 materials, YbMn Pn_2 are particularly unique due to the coupling between magnetism and

Dirac quasiparticles [25–28], unusual interlayer quantum coherent transport [1, 5], including promising attributes required for energy conversion technology like large thermoelectric power [32, 33] and giant anomalous Nernst effect [19]. Band structure calculations [1, 19, 20, 23, 30, 32] identified YbMn Pn_2 as nodal line semimetals, where Fermi surface (FS) consists of two Dirac-like bands and a heavy 3D-parabolic band. Despite these results pointing similar FS topology, experiments indicate differences between the FS of two compounds. Quantum oscillation studies [1, 6] in YbMnBi₂ detected two frequencies with Dirac-like dispersion and large carrier density ($\sim 10^{21}~{\rm cm}^{-3}$) comparable to other Weyl semimetals like Cd₃As₂ and NbP. In contrast, observation of a single quantum oscillation frequency [1, 5] and two orders of magnitude diminished carrier density [1, 5, 32] in YbMnSb₂ is difficult to reconcile within existing theoretical results.

In this Letter, we have used neutron and x-ray diffraction to characterize the proper magnetic and crystal structures of YbMnSb2 and investigate the correlation between the crystal/magnetic structures and FS topology via magnetic susceptibility, magnetotransport measurements and first principles calculation. We have identified that YbMnSb2 crystallizes in an orthorhombic Pnma structure with notable anti-phase displacement between the neighboring layers of the magnetic Mn ions. Band structure calculation, utilizing the newly obtained structural parameters, yields a reduced Brillouin zone (BZ) and more anisotropic FS topology of YbMnSb2 than the

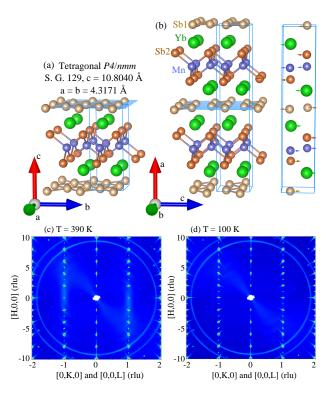


FIG. 1. (a) The reported tetragonal P4/nmm crystal structure of YbMnSb₂ as in Ref. [1, 5, 6, 27, 28, 30, 32, 33]. (b) The orthorhombic Pnma structure reported in this work. Arrows show the displacements of each atom along the a-axis of the tetragonal P4/nmm structure. The blue-shaded regions illustrate the Sb₁ layers. Blue rectangles highlight the unit cell. The contour plot of the neutron scattering intensity pattern of YbMnSb₂ at (c) T=390 K and (d) T=100 K in the (H,K,0) and (H,0,L) planes using the lattice parameters (21.58 Å, 4.3 Å, 4.3 Å).

Bi-based sister compound.

Earlier studies [1, 5, 6, 27, 28, 30, 32, 33] reported that YbMnSb₂ has a layered tetragonal P4/nmm structure [Fig. 1(a)]. However, the neutron scattering studies of YbMnSb₂ single crystal taken at $T=300~\mathrm{K}$ clearly shows the presence of notable reflections which should be absent in the tetragonal P4/nmm space group [6]. The origin of those forbidden reflections was not identified, partly due to the limited observable peaks. To reveal the proper crystal structure, we use the white beam neutron diffractometer Corelli covering a large volume in reciprocal space [35]. Figs.1(c) and (d) illustrate the contour map of the neutron scattering pattern obtained at T =390 K and T = 100 K. Note that Bragg reflections both in the (H,K,0) and (H,0,L) planes are observed due to the twinning of the crystal. Reflections at (2n+1,0,m)position, which corresponds to (integer, 0, half-integer L) in the P4/nmm cell, show considerable intensities and clearly indicate the doubling of c-axis parameter of the P4/nmm cell. In addition, a close examination of the reflection condition shows difference between equivalent reflections in the tetragonal space group, implying a lowering of the crystal structure symmetry, which is further confirmed by the single crystal x-ray diffraction. Both neutron and x-ray diffraction data can only be modeled and refined using an orthorhombic Pnma structure (space group No. 62) instead of a tetragonal P4/nmm structure. For analysis of structural refinements see the supplemental material (SM) Fig. S1 and Fig. S2 [36]. In the revised structure, Mn, Yb, and Sb ions are located at the 4c sites, all showing notable displacement along the c-axis [Fig. 1(b)]. The magnitude of the displacement increases as the system is cooled and leads to enhancement of the characteristic (2n+1,0,m) reflections.

After establishing the crystal structure, we now discuss the spin arrangement in $YbMnSb_2$. Fig. 2(a) shows the

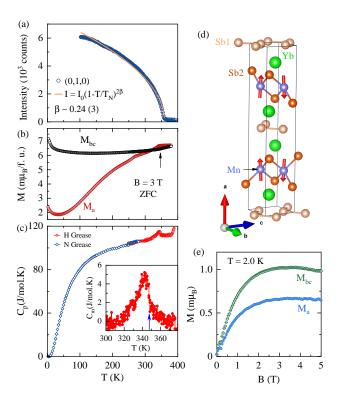


FIG. 2. Temperature dependence of (a) the (0,1,0) reflection peak as a magnetic order parameter, (b) zero-field cooled magnetization measured at 3 T, and (c) heat capacity, C_p , showing the AFM ordering temperature. Arrows indicate AFM transition temperature. (c) shows background subtracted C_p near the AFM transition. The yellow solid line in (a) represents a fit $I = I_0(1 - T/T_N)^{2\beta}$ to the data. $\beta \sim 0.24$ indicates a quasi 2D nature of magnetism. (d) The refined spin structure of the YbMnSb₂. The spin carries dominant a-axis component forming a C-type magnetic structure with finite c-axis component forming FM sheets coupled antiferromagnetically between the layers. (e) The extracted canted FM moment along the bc plane and the a-axis after subtracting the magnetic contribution from FM impurity and AFM order.

temperature dependence of peak intensity of the (0,1,0)magnetic reflection; it decreases sharply upon warming and becomes featureless background above the $T_{\rm N} \sim 350$ K, consistent with the transition determined from the magnetization and heat capacity [Figs. 2(b)-2(c)]. This implies a spin structure with a unit cell identical to the nuclear one and moments predominately perpendicular to the basal plane. For magnetic ions located at 4c site with propagation wavevector $q_m = (0,0,0)$, there are eight compatible magnetic space groups. Half of them can be excluded since the spin moments in those configurations are constrained within the basal plane, which contradicts the bulk magnetization data. For the remaining magnetic space groups Pn'm'a', Pnm'a', Pn'm'a, and Pnm'a, the refinement reveals that the magnetic space group Pn'm'a' provides the most satisfactory description of the diffraction data [Fig. 2(d)]. The Mn spin direction lies along the longest crystal axis, the a-axis, with a size of $\sim 3.17(3) \mu_{\rm B}$ in a collinear C-type AFM arrangement. Although the size of the estimated magnetic moment is similar to that previous report [6], it is smaller than the expected value for a full ordered Mn^{2+} (5 μ_{B}).

Spin canting, which is allowed from the magnetic space group, could be present since finite intensities were observed at (2n + 1, 0, 0). However, our polarized neutron experiments performed at room temperature revealed that a majority of the intensities originate from the nuclear component [Fig.S3 in SM[36]]. To estimate the canted moments accurately, magnetization measurements were performed. In Fig. 2(e), we plot the contribution of the canted FM moment to the magnetization after subtracting the contribution of the FM impurity and the AFM ordered state from the magnetization as described in the SM [36]. The maximum moment of $\sim 0.001 \ \mu_B$ is comparable with previous reports in YbMnSb₂ [6] and YbMnBi₂ [19] with a canting angle $\theta \sim 0.018^{\circ}$. This indicates a negligible canting of Mn moment away from the a-axis.

The orthorhombic Pnma space group enforces a zigzag arrangement of the Sb atoms [as in Fig. 1(b)] along the b-axis leading to a distorted Sb_1 layer similar to $(Ca/Sr/Ba/Eu)MnSb_2$ [9, 13, 17, 18, 37]. Despite the in-plane orthorhombicity $(b-c)/c \sim 0.31\%$ in YbMnSb₂ being several times smaller than that in AMnSb₂ materials, it is sufficient to drive an anisotropic FS compared to a tetragonal structure. In Fig. 3(a), we show the band structure for YbMnSb₂ with the collinear AFM arrangements of Mn spin and Pnma space group calculated using density functional theory (see SM for calculation details [36]) without considering spin-orbit coupling (SOC). The low energy band structure consists of heavier regular bands near the Γ -point and a linearly dispersing Diraclike band at the X point. The former arises from Mn dorbitals and Sb p-orbitals, whereas the latter mainly originates from the Sb p-orbitals. When SOC is taken into account, it has little effect on the bands near the Γ point

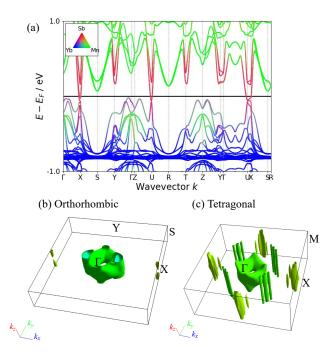


FIG. 3. (a) Momentum-dependent electronic structure of YbMnSb₂ in the orthorhombic Pnma space group with collinear AFM arrangement of Mn spins. Color represents the orbital contribution of each atom type as shown in the inset. Brillouin zone of YbMnSb₂ for (b) orthorhombic and (c) tetragonal structure showing the FS. For tetrgonal structure $E_{\rm F}$ is shifted by -50 meV. Due to doubling of unit cell volume, BZ volume in orthorhombic structure becomes half of tetragonal phase.

but dramatically increases the gap size at the X point [Fig. S5 in SM [36]]. Figs. 3(b) and 3(c) compare the BZ of YbMnSb₂ in orthorhombic and tetragonal structures, respectively. The FS in the undistorted tetragonal phase composes of two Dirac-like pockets; one electron-like near the X points and another hole-like along Γ -M line, and a big 3D hole pocket at the Γ point, in good agreement with several previous reports [19, 20, 30, 32]. However, due to in-plane orthorhombicity, the FS no longer exhibits the C_4 rotational symmetry . Moreover, the hole pocket along the Γ -M direction becomes gapped and the 3D hole pocket at Γ stretches along the Γ -X direction.

Fig. 4(a) shows the in-plane resistivity ρ_{xx} and the Hall coefficient R_H at 7 T in the temperature range 2 K to 390 K. With decreasing temperature, ρ_{xx} remains nearly flat down to $T_{\rm N}$ and decreases sharply below $T_{\rm N}$. $R_{\rm H}$ increases by an order of magnitude from 2.3×10^{-8} m³/C at 390 K to 2.43×10^{-7} m³/C at 250 K and decreases slightly on further cooling. The estimated carrier concentration $n_{\rm H} = |1/R_{\rm H}e| \sim 2.19 \times 10^{-19}$ cm⁻³ at 2 K is comparable with previous reports [1, 5], but two orders of magnitude smaller than YbMnBi₂ [6]. To obtain more insight, we measured the magnetic field dependence of ρ_{xx} [Fig. 4(b)] and the Hall resistivity ρ_{xy} [Fig. 4(c)]

at representative temperatures across the transition. At low temperatures, MR follows quadratic behavior in the low-field region and saturates at higher fields. For temperatures above 200 K, MR increases quadratically in the whole field region implying the multiple bands at the FS contribute to the charge transport. Consistent with previous results [1, 5], ρ_{xy} remains positive revealing that holes are dominant charge carriers. ρ_{xy} follows a linear increase up to 7 T for 300 K < T < 390 K but exhibits a concave upward increase below 250 K. Such nonlinear $\rho_{xy}(B)$ indicates that a relatively small number of highly mobile electron-like carriers contribute to the transport property as temperature decreases.

The magnetic field dependence of ρ_{xy} in a multi-band system is determined by the interplay of concentration and mobility of individual carriers. Hence, we analyzed the corresponding $\rho_{xx}(B)$ and $\rho_{xy}(B)$ employing the semiclassical two-band model as described in SM [36]. Figs. 4(d)-4(e) show the thermal evolution of the electron (hole) concentration $n_e(n_h)$ and electron (hole) mobility $\mu_e(\mu_h)$ extracted from the two-band model. The concentration of the hole carriers, n_h , is an order of magnitude larger than the electron-type carriers, n_e , while the mobility of the electron-like carriers, μ_e , is twice that of μ_h . Surprisingly, n_e and μ_e do not show strong temperature dependence. In contrast, n_h and μ_h display dramatic temperature dependence as they might be coming from the parabolic bands near the Γ points [in Fig. 3(b)]. Both, n_h falls and μ_h rises by two orders of magnitude across the magnetic transition suggesting that the hole pocket is partially gapped due to band folding as YbMnSb₂ transitions from PM to AFM ordered state.

To further deduce several important physical parameters related to the FS, we measured ρ_{xx} of another piece of crystal S#2 up to 16 T as shown in Fig. 4(f). As the magnetic field exceeds 6 T, prominent Shubnikov de Hass (SdH) quantum oscillations are detected. Fig. 4(g) presents the background subtracted $\Delta \rho_{xx}$ vs. 1/B showing the quantum oscillation at different temperatures up to 20 K. The corresponding fast Fourier transformation (FFT) reveals a primary frequency at $f_{\alpha} \simeq 70$ T [Fig. 4(h)], in good agreement with previous dHvA and SdH studies of YbMnSb₂ [1]. The frequency of quantum oscillation is related to the cross-section area S_F of FS perpendicular to the applied B direction via the Onsager relation, $S_F = (2\pi^2/\phi_0)F$, where ϕ_0 is the single magnetic flux quantum. Using this relation, S_F for f_{α} is estimated as 0.007 Å^2 , representing a tiny FS cross-sectional area of only 0.3% of the BZ area $(2\pi/b) \times (2\pi/c) = 2.12$ $Å^2$.

We also analyzed the SdH oscillations quantitatively using the Lifshitz-Kosevich (LK) formula [41, 42], which

predicts the oscillatory component of ρ_{xx} , $\Delta \rho$, as

$$\frac{\Delta\rho}{\rho(0)} \simeq \frac{5}{2} \left(\frac{\mu_0 H}{2F}\right)^{\frac{1}{2}} R_T(T) R_D(T_D) \cos\left[2\pi \left(\frac{F}{B} - \varphi\right)\right],\tag{1}$$

where $\rho(0)$ is the resistivity ρ_{xx} at B=0. The cosine term contains a phase factor $\varphi=\frac{1}{2}-\frac{\phi_B}{2\pi}-\delta$, in which ϕ_B is the Berry's phase and δ is related to FS curvature. $\delta=0$ for a smooth 2D cylinder, whereas $\delta=\pm 1/8$ for a 3D FS. In Eq.(1), the Landau level broadening and electron scattering result in two major damping factors, namely, the temperature damping factor $R_T(T)$ and the Dingle factor $R_D(T_D)$, respectively:

$$R_T(T) = \frac{2\pi^2 k_B T m^*}{\hbar e B} \sinh\left(\frac{2\pi^2 k_B T m^*}{\hbar e B}\right)$$
 (2)

and

$$R_D(T_D) = \exp\left(-\frac{2\pi^2 k_B T_D m^*}{\hbar e B}\right),\tag{3}$$

which are determined by the cyclotron effective mass m^* and the Dingle temperature T_D . Fitting of Eq.(2) to the thermal damping of FFT amplitude of f_{α} [inset of Fig. 4(h)] results the $m^* \sim 0.12 m_e$, similar to the previous reports [1, 5].

To identify the topological nature of f_{α} , the Landau level (LL) fan diagram is employed by plotting the $\Delta \rho_{xx}$ maxima in SdH oscillations against their associated LL index, n, in Fig. 4(i). The x-intercept of a linear fit to these data provides the accrued ϕ_B when the carrier completes one cyclotron orbit, via the relation, $\varphi = 1/2 - \phi_B/2\pi - \delta$. We assume $\delta = 0$, as previous SdH oscillation studies have established 2D nature of f_{α} [1, 5]. $\varphi = 0$ for a topologically nontrivial Berry's phase of π , while a trivial Berry's phase of 0 results in a $\varphi = 1/2$. A $\varphi = 0.001(4)$ in the present study indicates that the Fermi pocket giving rise to the SdH oscillations is consistent with having a topological origin and Dirac-like dispersion.

In summary, we have used neutron and x-ray single crystal diffraction, magnetic susceptibility, and magnetotransport measurements together with complementary band structure calculation to investigate the crystal and magnetic structure as well as the FS topology of YbMnSb₂. Both the x-ray and neutron diffraction unambiguously reveal that YbMnSb₂ crystallizes in an orthorhombic Pnma structure. Band structure calculation revealed a reduced BZ and more anisotropic FS of YbMnSb₂ compared to YbMnBi₂ because of in-plane orthorhombicity. The FS of YbMnSb₂ consisting of an anisotropic heavier regular band and a linearly dispersing Dirac-like band no longer exhibits the C_4 rotational symmetry as in undistorted YbMnBi₂. Analysis of SdH quantum oscillation reveals a non-trivial nature of tiny Fermi pocket consistent with Dirac-like energy-momentum dispersion.

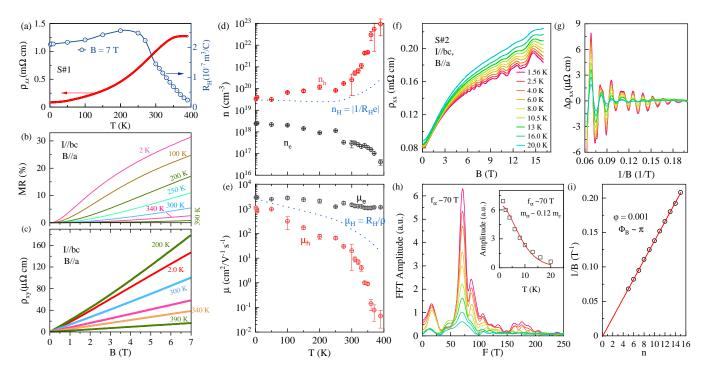


FIG. 4. (a) Temperature dependence of bc plane resistivity, ρ_{xx} , and Hall coefficient $R_{\rm H}$ at 7 T. Magnetic field dependence of (b) magnetoresistance defined as $[(\rho_{xx}(B) - \rho_{xx}(0))/\rho_{xx}(0)] \times 100$, and (c) the hall resistivity ρ_{xy} in the temperature range 2 to 390 K. Temperature variation of hole and electron (d) carrier concentration and (e) mobility estimated from the fitting of a two-band model to the MR and hall data. The blue dotted lines represent the carrier concentration, $n_{\rm H} = |1/R_{H}e|$, and mobility, $\mu = R_{\rm H}/\rho_{xx}$, estimated using one band model. (f) Field dependence of ρ_{xx} of crystal S#2 showing SdH quantum oscillations. (g) The corresponding background-subtracted $\Delta\rho_{xx}$ vs. 1/B. (g) FFT spectra of the $\Delta\rho_{xx}$ at different temperatures. Inset: LK fit (Equn.2) to the FFT amplitudes of the f_{α} . (h) Landau level fan diagram for f_{α} .

Acknowledgment: We are thankful to S. Nagasaki, D. Hamane, T. Miyake and T. Masuda for technical help during experiments. Also, we gratefully acknowledge fruitful discussion with M. tokunaga, K. Matsuyabashi and P. Shahi. This work was financially supported by the JSPS KAKENHI Grant number JP19H00648. A portion of this research used resources at SNS, a DOE Office of Science User Facility operated by the Oak Ridge National Laboratory. The polarized neutron scattering experiment at JRR-3 was carried out along the proposal No. 22401. The Fermi surfaces and band structure figures were respectively plotted using FermiSurfer [43] and pymatgen [44].

- [1] Kefeng Wang, D. Graf, Hechang Lei, S. W. Tozer, and C. Petrovic, Quantum transport of two-dimensional Dirac fermions in SrMnBi₂. Phys. Rev. B **84**, 220401(R) (2011).
- [2] Kefeng Wang, D. Graf, Limin Wang, Hechang Lei, S. W. Tozer, and C. Petrovic, Two-dimensional Dirac fermions and quantum magnetoresistance in CaMnBi₂, Phys. Rev. B 85, 041101(R) (2012).
- [3] Joonbum Park, G. Lee, F. Wolff-Fabris, Y. Y. Koh, M. J. Eom, Y. K. Kim, M. A. Farhan, Y. J. Jo, C. Kim, J. H. Shim, and J. S. Kim, Anisotropic Dirac Fermions in a

- Bi Square Net of SrMnBi₂, Phys. Rev. Lett. $\bf{107}$, 126402 (2011).
- [4] Y. J. Jo, Joonbum Park, G. Lee, Man Jin Eom, E. S. Choi, Ji Hoon Shim, W. Kang, and Jun Sung Kim, Valley-Polarized Interlayer Conduction of Anisotropic Dirac Fermions in SrMnBi₂, Phys. Rev. Lett. 113, 156602 (2014).
- [5] J. Y. Liu, J.Hu, D. Graf, T. Zou, M. Zhu, Y. Shi, S. Che, S.M.A. Radmanesh, C.N. Lau, L. Spinu, H.B. Cao, X.Ke, and Z.Q. Mao, Unusual interlayer quantum transport behavior caused by the zeroth Landau level in YbMnBi₂. Nat. Commun., 8(1), 646, (2017).
- [6] A. Wang, I. Zaliznyak, W. Ren, Lijun Wu, D. Graf, V. O. Garlea, J. B. Warren, E. Bozin, Y. Zhu, and C. Petrovic, Magnetotransport study of Dirac fermions in YbMnBi₂ antiferromagnet, Phys. Rev. B, 94, 165161 (2016)
- [7] Ya Feng, Zhijun Wang, Chaoyu Chen, Youguo Shi, Zhuojin Xie, Hemian Yi, Aiji Liang, Shaolong He, Junfeng He, Yingying Peng, Xu Liu, Yan Liu, Lin Zhao, Guodong Liu, Xiaoli Dong, Jun Zhang, Chuangtian Chen, Zuyan Xu, Xi Dai, Zhong Fang and X. J. Zhou, Strong Anisotropy of Dirac Cones in SrMnBi₂ and CaMnBi₂ Revealed by Angle-Resolved Photoemission Spectroscopy, Sci. Rep.,4, 5385 (2016).
- [8] J. Y. Liu, J. Hu, Q. Zhang, D. Graf, H. B. Cao, S. M. A. Radmanesh, D. J. Adams, Y. L. Zhu, G. F. Cheng, X. Liu, W. A. Phelan, J.Wei, M. Jaime, F. Balakirev, D. A. Tennant, J. F. DiTusa, I. Chiorescu, L. Spinu, and Z. Q. Mao, A magnetic topological semimetal Sr_{1-y}Mn_{1-z}Sb₂

- (y, z < 0.1), Nat. Mater., **16**, 905 (2017).
- [9] J. B. He, Y. Fu, L. X. Zhao, H. Liang, D. Chen, Y. M. Leng, X. M. Wang, J. Li, S. Zhang, M. Q. Xue, C. H. Li, P. Zhang, Z. A. Ren, and G. F. Chen, Quasi-two-dimensional massless Dirac fermions in CaMnSb₂, Phys. Rev. B, 95, 045128 (2017).
- [10] Anmin Zhang, Changle Liu, Changjiang Yi, Guihua Zhao, Tian-long Xia, Jianting Ji, Youguo Shi, Rong Yu, Xiaoqun Wang, Changfeng Chen and Qingming Zhang, Interplay of Dirac electrons and magnetism in CaMnBi₂ and SrMnBi₂, Nat. Commun., 7, 13833 (2016).
- [11] S. Huang, J. Kim, W. A. Shelton, E. W. Plummer, and R. Jin, Nontrivial Berry phase in magnetic BaMnSb₂ semimetal, Proc. Natl. Acad. Sci. USA, 114 6256, (2017).
- [12] Jinyu Liu, Jin Hu, Huibo Cao, Yanglin Zhu, Alyssa Chuang, D. Graf, D. J. Adams, S. M. A. Radmanesh, L. Spinu, I. Chiorescu, and Zhiqiang Mao, Nearly massless Dirac fermions hosted by Sb square net in BaMnSb₂, Sci Rep 6, 30525 (2016).
- [13] Changjiang Yi, Shuai Yang, Meng Yang, Le Wang, Yoshitaka Matsushita, Shanshan Miao, Yuanyuan Jiao, Jinguang Cheng, Yongqing Li, Kazunari Yamaura, Youguo Shi, and Jianlin Luo, Large negative magnetoresistance of a nearly Dirac material: Layered antimonide EuMnSb₂, Phys. Rev. B 96, 205103 (2017).
- [14] A. F. May, M. A. McGuire, and B. C. Sales, Effect of Eu magnetism on the electronic properties of the candidate Dirac material EuMnBi₂, Phys. Rev. B 90, 075109 (2014).
- [15] S. Borisenko, D. Evtushinsky, Q. Gibson, A. Yaresko, K. Koepernik, T. Kim, M. Ali, J. van den Brink, M. Hoesch, A. Fedorov, E. Haubold, Y. Kushnirenko, I. Soldatov, R. Schäfer and R. J. Cava, Time-reversal symmetry breaking type-II Weyl state in YbMnBi₂, Nat. Commun., 10, 3424 (2019).
- [16] H. Masuda, H. Sakai, M. Tokunaga, Y. Yamasaki, A. Miyake, J. Shiogai, S. Nakamura, S. Awaji, A. Tsukazaki, H. Nakao, Y. Murakami, T. Arima, Y. Tokura, S. Ishiwata1, Quantum Hall effect in a bulk antiferromagnet EuMnBi₂ with magnetically confined two-dimensional Dirac fermions. Sci. Adv., 2, e1501117 (2016).
- [17] J. Y. Liu, J. Yu, J. L. Ning, H. M. Yi, L. Miao, L. J. Min, Y. F. Zhao, W. Ning, K. A. Lopez, Y. L. Zhu, et al., Spin-valley locking and bulk quantum Hall effect in a noncentrosymmetric Dirac semimetal BaMnSb₂, Nat. Commun., 12, 4062 (2021)
- [18] H. Sakai, H. Fujimura, S. Sakuragi, M. Ochi, R. Kurihara, A. Miyake, M. Tokunaga, T. Kojima, D. Hashizume, T. Muro, et al., Phys. Rev. B 101, 081104(R) (2020).
- [19] Yu Pan, Congcong Le, Bin He, Sarah J. Watzman, Mengyu Yao, Johannes Gooth, Joseph P. Heremans, Yan Sun and Claudia Felser, Giant anomalous Nernst signal in the antiferromagnet YbMnBi₂, Nat. Mater., 21, 203 (2022).
- [20] Congcong Le, Claudia Felser, and Yan Sun, Design strong anomalous Hall effect via spin canting in antiferromagnetic nodal line materials, Phys. Rev. B, 104, 125145 (2021).
- [21] Xiao Li, Allan H. MacDonald, Hua Chen, Quantum Anomalous Hall Effect through Canted Antiferromagnetism, arXiv:1902.10650v1
- [22] Peng-Jie Guo, Zheng-Xin Liu, Zhong-Yi Lu, Quantum Anomalous Hall Effect in Antiferromagnetism,

- arXiv:2205.06702v1
- [23] Xiao-Sheng Ni, Cui-Qun Chen, Dao-Xin Yao, and Yusheng Hou, Origin of the type-II Weyl state in topological antiferromagnetic YbMnBi₂, Phys. Rev. B, 105, 134406 (2022).
- [24] R. Yang, M. Corasaniti, C. C. Le, Z. Y. Liao, A. F. Wang, Q. Du, C. Petrovic, X. G. Qiu, J. P. Hu, and L. Degiorgi, Spin-Canting-Induced Band Reconstruction in the Dirac Material Ca_{1-x}Na_xMnBi₂, Phys. Rev. Lett. **124**, 137201 (2020).
- [25] A. Sapkota, L. Classen, M. B. Stone, A. T. Savici, V. O. Garlea, Aifeng Wang, J. M. Tranquada, C. Petrovic, and I. A. Zaliznyak, Signatures of coupling between spin waves and Dirac fermions in YbMnBi₂. Phys. Rev. B, 101, 041111(R) (2020).
- [26] J. -R. Soh, H. Jacobsen, B. Ouladdiaf, A. Ivanov, A. Piovano, T. Tejsner, Z. Feng, H. Wang, H. Su, Y. Guo, Y. Shi, and A. T. Boothroyd, Magnetic structure and excitations of the topological semimetal YbMnBi₂. Phys. Rev. B, 100, 144431 (2019).
- [27] X. Hu, A. Sapkota, Z. Hu, A. T. Savici, A. I. Kolesnikov, J. M. Tranquada, C. Petrovic, and I. A. Zaliznyak, Coupling of magnetism and Dirac fermions in YbMnSb₂, Phys. Rev. B. 107, L201117 (2023).
- [28] S. M. Tobin, J.-R. Soh, H. Su, A. Piovano, A. Stunault, J. A. Rodríguez-Velamazán, Y. Guo, and A. T. Boothroyd, Magnetic excitations in the topological semimetal YbMnSb₂, Phys. Rev. B. 107, 195146 (2023).
- [29] R. Kealhofer, S. Jang, S. M. Griffin, C. John, K. A. Benavides, S. Doyle, T. Helm, P. J. W. Moll, J. B. Neaton, J. Y. Chan, J. D. Denlinger, and J. G. Analytis, Observation of a two-dimensional Fermi surface and Dirac dispersion in YbMnSb₂, Phys. Rev. B. 97, 045109 (2018).
- [30] Ziyang Qiu, Congcong Le, Zhiyu Liao, Bing Xu, Run Yang, Jiangping Hu, Yaomin Dai, and Xianggang Qiu, Observation of a topological nodal-line semimetal in YbMnSb₂ through optical spectroscopy, Phys. Rev. B 100, 125136 (2019)
- [31] Y.-Y. Wang, Yi-Yan Wang, Sheng Xu, Lin-Lin Sun, and Tian-Long Xia, Quantum oscillations and coherent interlayer transport in a new topological Dirac semimetal candidate YbMnSb₂, Phys. Rev. Mater., 2, 021201(R) (2018).
- [32] Y. Pan, F.-R. Fan, X. Hong, B. He, C. Le, W. Schnelle, Y. He, K. Imasato, H. Borrmann, C. Hess, B. Büchner, Y. Sun, C. Fu, G. Jeffrey Snyder, and C. Felser, Thermoelectric Properties of Novel Semimetals: A Case Study of YbMnSb₂, Adv. Mater. 33, 2003168 (2021).
- [33] S. Baranets and S. Bobev, Transport properties and thermal behavior of YbMnSb₂ semimetal above room temperature. Journal of Solid State Chemistry, 303, 122467 (2021).
- [34] J.-R. Soh, S. M. Tobin, Hao Su, I. Zivkovic, B. Ouladdiaf, A. Stunault, J. Alberto Rodríguez-Velamazán, K. Beauvois, Y. Guo, and A. T. Boothroyd, Magnetic structure of the topological semimetal YbMnSb₂, Phys. Rev. B, 104, L161103 (2021).
- [35] F. Ye, Y. Liu, R. Whitfield, R. Osborn, and S. Rosenkranz, J. Appl. Crystallogr. 51, 315 (2018).
- [36] See Supplemental Material for details pertaining to sample synthesis, experimental methods and techniques, Rietveld refinements, polarized neutron scattering, DFT result with SOC, estimation of the spin canting moment, and analysis of magnetotransport data using semiclassi-

- cal two-band model.
- [37] Dongliang Gong, Silu Huang, Feng Ye, Xin Gui, Jiandi Zhang, Weiwei Xie, and Rongying Jin, Canted Eu magnetic structure in EuMnSb₂, Phys. Rev. B, 101, 224422 (2020).
- [38] T. M. Michels-Clark, A. T. Savici, V. E. Lynch, X. Wang, and C. M. Hoffmann, J. Appl. Crystallogr. 49, 497 (2016).
- [39] A. Wills, Physica B **276–277**, 680 (2000).
- [40] J. Rodríguez-Carvajal, Physica B **192**, 55 (1993).
- [41] Landwehr G. and Rashba, E. I., Landau Level Spectroscopy: Modern Problems in Condensed Matter Sciences Vol. 27.2 (North-Holland, (1991).
- [42] Shoenberg, D., Magnetic Oscillations in Metals. (Cambridge Univ. Press, 1984).
- [43] Kawamura, M., Comput. Phys. Commun. 239, 197 (2019).
- [44] Shyue Ping Ong, William Davidson Richards, Anubhav Jain, Geoffroy Hautier, Michael Kocher, Shreyas Cholia, Dan Gunter, Vincent Chevrier, Kristin A. Persson, Gerbrand Ceder. Python Materials Genomics (pymatgen): A Robust, Open-Source Python Library for Materials Analysis. Computational Materials Science, 68, 314–319, (2013).

SUPPLEMENTAL MATERIAL

Single crystal growth, experimental methods and techniques

We have prepared large single crystals of YbMnSb₂ using antimony as a flux. The high-purity elements of Yb, Mn, and Sb with a 1:1:4 stoichiometric ratio were placed in an alumina crucible as starting materials. To grow the single crystals we followed the recipe as described in Ref. [1]. The as-grown single crystals were extensively characterized by single crystal x-ray and neutron diffraction at room temperature and energy dispersive x-ray analysis (EDX). To check the chemical homogeneity of the crystal, EDX spectra obtained at several randomly selected spots from the samples were analyzed. The analyses show that the crystals are chemically homogeneous within the limit of EDX with an average stoichiometric ratio, Yb: Mn: Sb = 0.98:1.01:2.01.

A rectangular piece of YbMnSb₂ single crystal was cut for magnetic susceptibility measurement in a Superconducting Quantum Interference Device (MPMS XL, Quantum Design). The electrical resistivity and heat capacity measurements in the temperature range between 2 to 390 K were performed using a Quantum Design Physical property measurement system. For Shubnikov-de Hass (SdH) quantum oscillation measurements up to 16 T an oxford superconducting magnet is used.

Neutron diffraction measurements were performed on the SNS CORELLI Beamline-09 installed at Oak Ridge National Laboratory, USA using a piece of single crystal with a weight of ~ 100 mg. The single crystal was cooled down using a closed-cycle He4 refrigerator. Data reduction and analysis were conducted using MANTID software [2]. Magnetic structures were analyzed with SARAH software [3]. All the refinements of the neutron scattering data were performed with FULLPROF software [4].

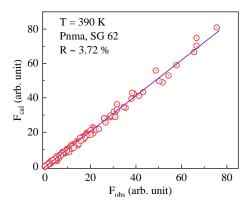


Fig.S 1. The results of refinements of the neutron scattering intensity at T=390 K with the orthorhombic structure and Pnma space group no. 62.

TABLE I. Refined structural parameters for YbMnSb₂ from neutron diffraction at 390 K in the orthorhombic Pnma space group, with a=21.5963(8) Å, b=4.3235(17) Å, c=4.3099(13) Å, $\alpha=\beta=\gamma=90^{\circ}$. Unit cell volume V=402.43(2) Å³, Number of formula unit per unit cell Z=4.

Atoms	Wyckoff position	X	У	\mathbf{z}
Yb	4c	0.38612(4)	1/4	0.2629(2)
Sb1	4c	0.00099(9)	3/4	0.2677(3)
Sb2	4c	0.32985(7)	3/4	0.7627(2)
Mn	4c	0.2498(3)	3/4	0.2646(6)

Single crystal neutron and x-ray diffraction

The neutron scattering pattern at T = 390 K is successfully refined assuming the orthorhombic structure with Pnma space group no.62 as evidenced by the good agreement between calculated structure factor square (F_{cal}^2) and observed structure factor square (F_{obs}^2) [in Fig.S1]. To further confirm, we checked the single crystal x-ray diffraction of YbMnSb₂ (with a typical crystal size ~ 60 μ m) at T = 250 K. Figs.S2(a) and (b) show the single crystal x-ray diffraction patterns in the (H,K,0) and (H,0,L) reciprocal planes, respectively. Reflections in the former plane satisfies the necessary reflection condition H=2n for the Pnma space group No.62. Note that the sample used in this x-ray experiment was nearly single domained. Therefore, the (H,0,L) reflections from the other twin were weak [Fig.S2]. The refinement of the x-ray diffraction indeed ascertain that YbMnSb₂ crystallizes in orthorhombic Pnma structure rather than the tetragonal centrosymmetric P4/nmm suggested in previous reports [1, 5, 6]. As can be seen in Fig.S2(c), the F_{cal}^2 matches very well with the F_{obs}^2 , indicating excellent structure refinement. The details of the refined crystal structural parameters are given in Table.I.

Polarized neutron scattering

We performed polarized neutron scattering measurements at the polarized neutron triple-axis spectrometer (PONTA) installed in JRR-3. The spectrometer was operated in the P_{xx} longitudinal polarization analysis mode, in which the direction of the neutron spin polarization, p_N , was set to be parallel or antiparallel to the scattering vector, $Q = k_i - k_f$ by guide fields and a spin flipper. We measured intensities of spin-flip (SF) and nonspin-flip (NSF) scattering processes, in which the spins of the incident neutrons were flipped and remained unchanged, respectively. In the present setup, magnetic and nuclear scattering signals should be separated from each other, and observed in the SF and NSF channels, respectively. Figs.S3(a) and (b) show the rocking curve

profiles of the (4,0,0) and (3,0,0) reflections, respectively, at room temperature. As shown in Fig.S3(a), the NSF scattering dominate over the SF scattering at the (4,0,0) reflection, which confirms that the (4,0,0) fundamental reflection does not contain magnetic components. Very weak intensities in the SF channel are due to the imperfect polarization of the incident neutron beam. We found that the NSF scattering was also stronger in the (3,0,0) superlattice reflection as shown in Fig.S3(b), suggesting that the origin of this superlattice reflection is mainly attributed to the nuclear component. Note that the intensities at (3,0,0) contain a very small half-lambda contamination, which equally contributes to both the SF and NSF intensities.

Spin canting moment from magnetization

In Fig.2(b) of the main text, we show the temperature dependence of the magnetization M_{bc} and M_a of the YbMnSb₂ measured at H = 3 T, respectively. The temperature dependence of magnetizations and the estimated transition temperature from the temperature dependence of the magnetization M_{bc} and M_a are consistent with previous reports [1, 6]. With decreasing temperature, M_{bc} and M_a bifurcates below $T_N \sim 345$ K; M_a decrease rapidly, whereas M_{bc} reveals weak temperature dependence. Below 30 K, both M_{bc} and M_a reveal a weak upturn as temperature decreases. Fig.S4(a) and (b) show the field dependence of the M_{bc} and M_a at T= 2.0 K and T = 370 K, respectively. In the PM state at T = 370 K, both M_{bc} and M_a clearly overlap on top of each other, whereas below $T_{\rm N}$, the difference between M_{bc} and M_a start to grow with decreasing temperature. The persistence of FM signal below B < 0.5 T even in the PM state implies that the weak upturn in M_{bc} and M_a at low temperatures is likely to arise from a trace amount of MnSb₂ impurity in the sample.

To extract the size of intrinsic magnetic moment arising from the canting of spin, we followed a method as explained below. For simplicity, we only describe the procedure applied for $B \parallel a$ -axis. Figs.S5(a) and (b) show the field dependence of the magnetization of YbMnSb₂ at T = 370 K and T = 2 K, respectively. The experimental data M_{exp} in PM state (T = 370 K) can be assumed as the sum of the magnetization arising from the FM impurity, $M_{\rm FMi}$, and the PM state, $M_{\rm PM}$ as shown in Fig.S5(a). The magnetic contribution from the $M_{\rm FMi}$ is estimated by subtracting the $M_{\rm PM}$ from $M_{\rm exp}$ following a similar method used to extract the contribution of FM impurity in iron based single crystals [7]. To calculate the $M_{\rm PM}$, as shown in Fig.S5(a), a linear fit to the $M_{\rm exp}$ data in the field range 1 T to 5 T is applied and extrapolated to zero. By making the finite intercept to zero, the linear line passing through the origin can be assumed as the magnetization due to $M_{\rm PM}$.

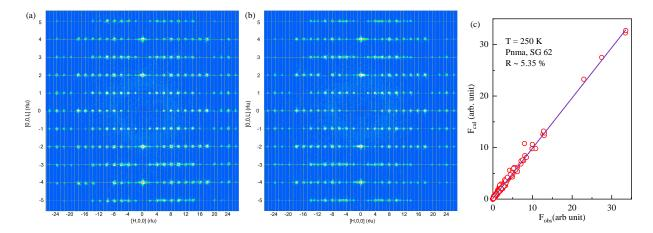


Fig.S 2. Image of single crystal x-ray diffraction patterns of YbMnSb₂ at T=250 K (a) in the (H,K,0) plane satisfying the reflection condition H=2n for the Pnma space group, and (b) in the (H,0,L) plane confirming the doubling of unit cell along the a-axis. (c) The refinements of the x-ray diffraction pattern at T=250 K with the orthorhombic structure and Pnma space group no. 62.

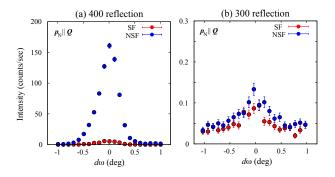


Fig.S 3. Polarized neutron scattering profiles of (a) (4,0,0) and (b) (3,0,0) reflections measured at room temperature. The beam polarization was 0.928.

However, in the AFM ordered state, in addition to $M_{\rm FMi}$, the $M_{\rm exp}$ will also contain contributions from the AFM ordered state (M_{AFM}) and the canted FM component (M_{CFM}) . Therefore, to estimate the M_{CFM} a two step procedure is followed. First, following a similar method used to extract $M_{\rm PM}$ at $T>T_{\rm N},\,M_{\rm AFM}$ at 2 K is extracted by performing the linear fit in the field range 2.5 T to 5 T. After subtraction of M_{AFM} from M_{exp} , the residue will contain the total FM component of magnetization, M_{FM}^{T} arising from the M_{CFM} and M_{FMi} as shown in Fig.S5(b). As $M_{\rm FMi}$ is expected to saturate with decreasing temperature, the estimated $M_{\rm FMi}$ at $T=370~{\rm K}$ provides a good approximation of the $M_{\rm FMi}$ even at lower temperatures. Therefore, in the second step, we extract the intrinsic M_{CFM} , by subtracting the $M_{\text{FM}i}$ at T=370K from the $M_{\rm FM}^{\rm T}$ as shown in Fig.S5(c). A similar strategy is followed to estimate the spin canting moment for magnetic field along the bc plane.

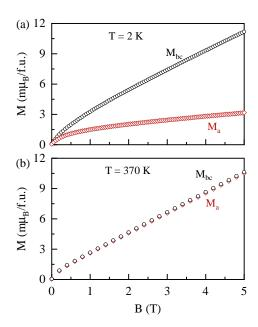


Fig.S 4. Magnetic field dependence of M_{bc} and M_a at (a) $T=2~{\rm K}$ in the AFM ordered state, and (c) at $T=370~{\rm K}$ in the paramagnetic state.

Electronic band structure

The density functional theory calculations for the band structure and Fermi surfaces (Fig. 3 in the main text) were performed using VASP code [8] using the GGA-PBE approximation [9] with the structure fixed to that determined experimentally in this work. The projector-augmented wave method [10] was employed to describe ion-electron interactions. The energy cutoff was set to 600 eV for the plane wave expansion of the wave functions, and a $2\times10\times10$ k-point mesh was used for the Bril-

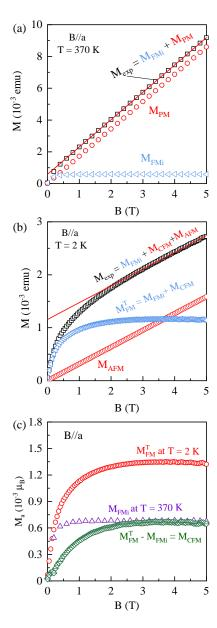


Fig.S 5. The field dependence of the magnetization at (a) $T=370~\rm K$ and (b) $T=2~\rm K$ for magnetic field applied parallel to a-axis. The red lines represent the linear fit to the data at high field region. The black square (\square), red circle (\bigcirc) and blue triangle (\triangleleft) represent the experimental data, $M_{\rm exp}$, PM/AFM contribution, $M_{\rm PM/AFM}$, and the contribution from FM impurity, $M_{\rm FMi}$ or $M_{\rm FMi}^{\rm T}$, respectively. (c) The extracted FM contribution arising from the canted moment after subtracting the magnetization from the FM impurity and AFM order at $T=2~\rm K$.

louin zone integration for the self consistent calculations. The rotationally invariant DFT+U approach of Dudarev et al.[11] was used with $U_{\rm f}=4$ eV for Yb to reproduce photoemission spectra as per Ref. [5]. A non-self consistent calculation with fixed electronic density was performed to obtain eigenvalues along high-symmetry lines for the band structure and on a dense uniform mesh for

the Fermi surface calculations. Fig.S6 in this supplement shows the theory calculated band structure for YbMnSb₂ with spin-orbit coupling in the collinear AFM arrangements of Mn spin, while Fig. 3 in the main text was obtained from calculations without spin-orbit coupling.

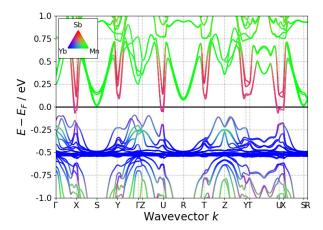


Fig.S 6. Electronic band structure of YbMnSb₂ with the orthorhombic structure and the collinear C-type AFM arrangement of Mn spins including the spin orbit coupling.

Analysis of magnetoresistance using a two-band model

To extract the carrier concentrations and mobilities of individual bands, we analyzed the magnetic field dependence of ρ_{xx} and ρ_{xy} at different temperatures employing the semiclassical two-band model. Based on this model $\rho_{xx}(B)$ and $\rho_{xy}(B)$ are described as

$$\rho_{xx}(B) = \frac{1}{e} \frac{(n_h \mu_h + n_e \mu_e) + n_h \mu_e (n_h \mu_e + n_e \mu_h) B^2}{(n_h \mu_h + n_e \mu_e)^2 + \mu_h^2 \mu_e^2 (n_h - n_e) B^2}$$
(4)

and

$$\rho_{xy}(B) = \frac{1}{e} \frac{(n_h \mu_h^2 - n_e \mu_e^2) + \mu_h^2 \mu_e^2 (n_h - n_e) B^2}{(n_h \mu_h + n_e \mu_e)^2 + \mu_h^2 \mu_e^2 (n_h - n_e) B^2} B, \quad (5)$$

where $n_e(n_h)$ and $\mu_e(\mu_h)$ correspond to electron (hole) concentration and electron (hole) mobility, respectively. In Figs.S7 (a)-(d), we show the typical examples of simultaneous fitting of Equn.4 and Equn.5 to $\rho_{xx}(B)$ and $\rho_{xy}(B)$, where they show nonlinear field dependence, respectively.

 Y.-Y. Wang, Yi-Yan Wang, Sheng Xu, Lin-Lin Sun, and Tian-Long Xia, Quantum oscillations and coherent interlayer transport in a new topological Dirac semimetal candidate YbMnSb₂, Phys. Rev. Materials, 2, 021201(R) (2018).

- [2] T. M. Michels-Clark, A. T. Savici, V. E. Lynch, X. Wang, and C. M. Hoffmann, J. Appl. Crystallogr. 49, 497 (2016).
- [3] A. Wills, Physica B **276–277**, 680 (2000).
- [4] J. Rodríguez-Carvajal, Physica B 192, 55 (1993).
- [5] R. Kealhofer, S. Jang, S. M. Griffin, C. John, K. A. Benavides, S. Doyle, T. Helm, P. J. W. Moll, J. B. Neaton, J. Y. Chan, J. D. Denlinger, and J. G. Analytis, Observation of a two-dimensional Fermi surface and Dirac dispersion in YbMnSb₂, Phys. Rev. B. 97, 045109 (2018).
- [6] J.-R. Soh, S. M. Tobin, Hao Su, I. Zivkovic, B. Ouladdiaf, A. Stunault, J. Alberto Rodríguez-Velamazán, K. Beauvois, Y. Guo, and A. T. Boothroyd, Magnetic structure of the topological semimetal YbMnSb₂, Phys. Rev. B, 104, L161103 (2021).
- [7] David C. Johnston, The puzzle of high temperature superconductivity in layerediron pnictides and chalcogenides, Advances in Physics, **59**, 803 (2010)
- [8] G. Kresse and J. Furthmüller, Phys. Rev. B 54, 11169 (1996).
- [9] J. P. Perdew, K. Burke, and M. Ernzerhof, Phys. Rev. Lett. 77, 3865 (1996).
- [10] P. E. Blöchl, Phys.Rev.B **50**, 17953 (1994).
- [11] S. L. Dudarev, G. A. Botton, S. Y. Savrasov, C. J. Humphreys, and A. P. Sutton, Phys. Rev. B 57, 1505

(1998).

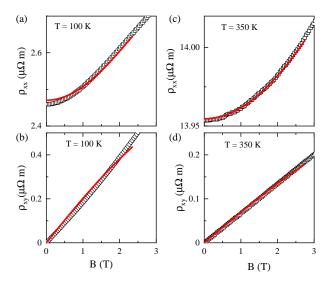


Fig.S 7. (a) and (b) shows the simultaneous fitting of Equn.4 and Equn.5 to the ρ_{xx} and ρ_{xy} data at T=100 K. The fitting for ρ_{xx} and ρ_{xy} at T=350 K are shown in (c) and (d), respectively